IEEE Access
Multidisciplinary ⋮ Rapid Review ⋮ Open Access Journal

Received September 11, 2019, accepted October 5, 2019, date of publication October 9, 2019, date of current version October 23, 2019.

Digital Object Identifier 10.1109/ACCESS.2019.2946406

Screw Insertion Method in Peg-in-Hole Assembly for Axial Friction Reduction

ZHI LIU[1], LIBIN SONG[1], ZHIMIN HOU[1], KEN CHEN[1], SHAOLI LIU[2], AND JING XU[1], (Member, IEEE)

[1]State Key Laboratory of Tribology, Department of Mechanical Engineering, Beijing Key Laboratory of Precision/Ultra-Precision Manufacturing Equipment Control, Tsinghua University, Beijing 100084, China
[2]School of Mechanical Engineering, Beijing Institute of Technology, Beijing 100081, China

Corresponding author: Jing Xu (jingxu@tsinghua.edu.cn)

This work was supported in part by the National Key Research and Development Program of China under Grant 2017YFC0822204, in part by the National Natural Science Foundation of China (NSFC) under Grant U1613205 and Grant 51675291, and in part by the State Key Laboratory of China under Grant SKLT2018C04.

ABSTRACT Peg-in-hole is one of the most frequent mating features between parts, where the large friction resistance and poor contact situations result in the failure of part mating. To address this problem, this paper proposes a screw insertion method in peg-in-hole assembly for axial friction reduction. First, the effect of screw motion on axial friction reduction is analyzed with point contact and face contact. Second, the screw insertion method in clearance-fit peg-in-hole assembly with point contact is discussed; this method works better than the conventional linear insertion method for jamming prevention; the reciprocate screw insertion strategy is also investigated to reduce the influence of axis offset on screw insertion. Third, the screw insertion method in interference-fit peg-in-hole assembly with face contact is discussed. Finally, axial friction reduction is validated with experiments of point contact with screw motion and experiments of screw insertion in clearance-fit and interference-fit peg-in-hole assembly.

INDEX TERMS Peg-in-hole assembly, screw motion, friction reduction, robotic assembly.

I. INTRODUCTION

Assembly is a capstone process in manufacturing [1], and peg-in-hole is one of the most frequent mating features between parts, which is also the basic and vital problem for robotic assembly [2]. Most failures of robotic peg-in-hole assembly occur because of large contact forces and poor contact situations between the peg and hole.

To address this problem, researchers concentrate on contact state analysis and motion control of the peg-in-hole process. For contact state analysis, Simunovic [3] discussed a key ill situation for constrained insertion called jamming, in which the peg sticks in the hole because of a wrong proportion of forces and moments applied to the peg. Whitney [4] built the quasi-static model of the mating process and graphically demonstrated force equilibrium conditions for all the contact states in a jamming diagram. Like the friction cone, the jamming diagram is closely related to the friction coefficient μ, as shown in Fig. 1, and describes the relative moveability between the mating parts. Researchers utilize this graphic technique to analyze the feasible motions and feasible regions of the applied forces to prevent jamming [5], [6], and to design compliant devices for the required assembly environment [7].

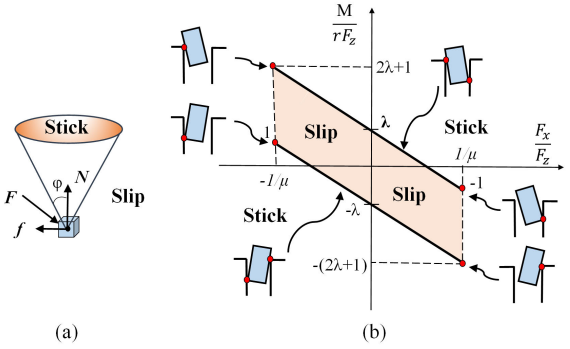

FIGURE 1. (a) Friction cone, (b) jamming diagram.

For motion control, many researchers put effort into interaction control of peg-in-hole process instead of position control. Mechanical devices with passive compliance, like

The associate editor coordinating the review of this manuscript and approving it for publication was Gursel Alici.

the remote center compliance (RCC) wrist, are designed to accommodate to the misalignment error; and the active compliance approaches, like hybrid force/position control [8] and impedance control [9], utilize the measurement of contact force and moment for active compliant motion to prevent contacts between mating parts [10], which are more suitable for complex assembly tasks. Besides interaction control approaches, some researchers also pay attention to the motion strategy of the manipulated peg to assist the peg-in-hole assembly. Chhatpar and Branicky [11] presented a spiral path based blind search strategy for the hole position in order to overcome the position uncertainty. Li and Qiao [12] proposed a crankshaft-bearing insertion strategy based on the theory of attractive region in environment to obtain sensor-less assembly. Balletti *et al.* [13] implemented an induced oscillation motion in insertion phase without any force measurement to avoid jamming, but this approach can not guarantee the boundary of contact forces, and the large mating clearance of 0.5 mm in the experiments may be not suitable for high precision assembly. Unlike onefold motion strategy, Baksys *et al.* [14] introduced the vibration motion along the axial direction to the RCC device for parts alignment, but the lateral and axial compliance parameter must be well tuned for specific applications.

This paper is aimed at combining the motion strategy with conventional interaction control approach to actively reduce the frictional force in the axial direction and to obtain better contact situations of the peg-in-hole assembly. For friction reduction, many researchers have investigated methods with lubrication and antifriction materials, and some researchers pay attention to further friction reduction methods by actively imposing the additional motions. Godfrey [15] and Yoo and Kim [16] investigated the friction reduction phenomenon using mechanical vibrations with high frequency and small amplitude, and vibrations normal [17] and tangential [18] to the contact surface were both analyzed with Coulomb and Dahl friction models. But the vibration should be excited by a vibrator with frequency that reaches several kHz, making this method difficult to apply to conventional industrial tasks. In this paper, a screw motion strategy is designed to utilize the effect of friction reallocation to control the frictional force in specific direction. By imposing a screw motion around cylindrical axis of the peg, frictional force in axial direction can be reduced with specific screw motion parameter.

In this paper, we propose a screw insertion method for peg-in-hole assembly, which combines the screw motion strategy with the conventional motion control approaches to reduce the axial frictional force, resulting in an increased area of jamming quadrangle and decreased jamming possibility. The principle of axial friction reduction and applications for both interference-fit and clearance-fit peg-hole assembly are analyzed, and comparative experiments for linear and screw motion strategy were implemented for interference-fit assembly based on position control and clearance-fit assembly based on impedance control.

The remainder of the paper is organized as follows. Section II proposes the screw insertion method of peg-in-hole assembly with axial friction reduction. Section III discusses the screw insertion in peg-hole assembly with clearance fit. Section IV discusses the screw insertion in peg-hole assembly with interference fit. Section V includes experiments to verify the results derived above. Section VI concludes with a discussion of future research directions.

II. SCREW INSERTION METHOD FOR AXIAL FRICTION REDUCTION

In the conventional peg-in-hole assembly controlled by passive compliance or the active compliance approach, the actual trajectory of the manipulated workpiece is nearly a 5-DOF $(x, y, z, \theta_x, \theta_y)$ motion, as shown in Fig. 2, and the rotation around the axial(insertion) direction is almost stationary, this motion strategy is called linear insertion in this paper. In contrast, the screw motion strategy utilizes the 6th DOF θ_z to obtain axial friction reduction by imposing an additional axial rotation on the conventional linear insertion along the peg axis.

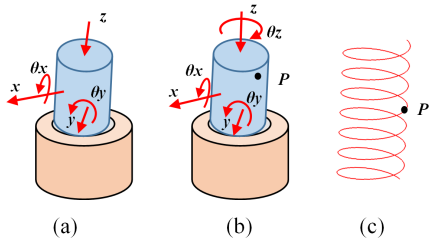

FIGURE 2. (a) Conventional linear insertion, (b) proposed screw insertion, (c) screw motion of points on the peg.

The principle of axial friction reduction will be derived for both point contact and face contact situations between a screw moving cylinder and the contacted geometry.

A. AXIAL FRICTION REDUCTION OF POINT CONTACT

Without loss of generality, we consider two situations of point contact between a rigid cylinder and a stationary rigid geometry.

Fig. 3(a) shows contact at the side surface, where the side surface of the cylinder is tangent to the geometry at point C. The cylinder takes a screw motion that combines a rotation around the cylindrical axis and a translation along the cylindrical axis. The motion of a point fixed on the cylinder can be described with twist $\boldsymbol{\xi} = (\boldsymbol{v}, \boldsymbol{w})$, where $\boldsymbol{w}$ is the angular velocity and $\boldsymbol{v}$ is linear component of screw motion; the pitch of screw motion can be expressed as:

$$h = \frac{\boldsymbol{w} \cdot \boldsymbol{v}}{\|\boldsymbol{w}\|^2} = \frac{v_a}{w} \tag{1}$$

where $\boldsymbol{v}_a$ is the axial linear velocity of the screw motion along the cylindrical axis.

Build coordinate frame $O - XYZ$ with the YOZ plane crossing contact point C and the cylindrical axis; the Z-axis

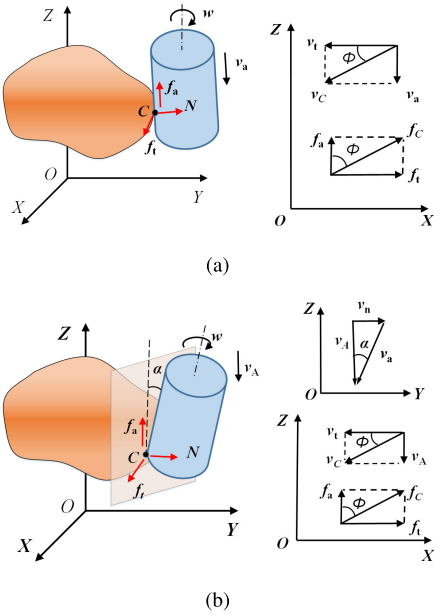

FIGURE 3. Point contact of cylinder and geometry: (a) contact at side surface of cylinder, (b) contact at the edge of side surface of cylinder.

is parallel to cylindrical axis, and then, the relationship of instantaneous tangential velocity $\boldsymbol{v}_t$, axial linear velocity $\boldsymbol{v}_a$ and resultant velocity $\boldsymbol{v}_C$ of point C can be expressed as:

$$v_a = v_C \cos\phi \tag{2}$$

$$v_t = v_C \sin\phi \tag{3}$$

where ϕ is the angle between $\boldsymbol{v}_t$ and $\boldsymbol{v}_a$.

There are frictions from two directions at the contact point: axial frictional force $\boldsymbol{f}_a$, generated by relative translation along the axis between parts, and tangential frictional force $\boldsymbol{f}_t$, generated by relative rotation around the axis. The resultant friction $\boldsymbol{f}_C$ follows the Coulomb's friction law as $f_C = \mu N$, where $\boldsymbol{N}$ is the normal force; then, we can obtain:

$$f_a = \mu N \cos\phi \tag{4}$$

$$f_t = \mu N \sin\phi. \tag{5}$$

Combining Equations(1)-(5), we obtain the relationship of frictions and the screw pitch h and cylinder radius r as:

$$\frac{f_a}{f_t} = \frac{\|\boldsymbol{v}_a\|}{\|\boldsymbol{v}_t\|} = \frac{v_a}{wr} = \frac{h}{r}. \tag{6}$$

Define $\mu_a = \mu\cos\phi$ and $\mu_t = \mu\sin\phi$, called the equivalent tangential friction coefficient and equivalent axial friction coefficient, respectively, in this paper; then, Equations (4) and (5) can be simplified as:

$$f_a = \mu_a N \tag{7}$$

$$f_t = \mu_t N. \tag{8}$$

Additionally, μ_a, μ_t can be calculated by:

$$\mu_a = \frac{h}{\sqrt{h^2 + r^2}}\mu \tag{9}$$

$$\mu_t = \frac{r}{\sqrt{h^2 + r^2}}\mu. \tag{10}$$

Fig. 3(b) shows contact point C at the bottom edge of the side surface of the cylinder. The angle between the cylindrical axis and tangent plane is constant as α. The cylinder takes the composite motion of rotation around the cylindrical axis and translation along the projection of the cylindrical axis on the tangent plane, which can also be seen as a composite motion of the screw motion around the cylindrical axis and translation along the normal of the tangent plane.

Build coordinate frame $O - XYZ$ with the YOZ plane crossing C and cylindrical axis; the Z-axis is parallel to the projected line on the tangent plane. Then, the linear velocity along the projected line $\boldsymbol{v}_A$ and axial linear velocity $\boldsymbol{v}_a$ are related by:

$$v_A = v_a \cos\alpha. \tag{11}$$

Similarly, the axial frictional force $\boldsymbol{f}_a$ and tangential frictional force $\boldsymbol{f}_t$ can be expressed by:

$$\begin{cases} \dfrac{f_a}{f_t} = \dfrac{v_A}{wr} = \dfrac{h}{r}\cos\alpha \\ f_a = \mu_a N \\ \mu_a = \dfrac{h\cos\alpha}{\sqrt{(h\cos\alpha)^2 + r^2}}\mu. \end{cases} \tag{12}$$

Equations (6), (7), (9), and (12) show that when the cylinder takes a screw motion with point contacts with a stationary geometry, the resultant friction is reallocated by the screw motion, where the ratio of axial frictional force f_a and tangential frictional force f_t is proportional to the pitch h and in inverse ratio to radius r.

B. AXIAL FRICTION REDUCTION OF FACE CONTACT

Next, we extend the axial friction reduction of screw motion with point contact to face contact.

Without loss of generality, we consider the situation shown in Fig. 4; the cylinder makes face contact with the stationary coaxial cylinder hole, and the cylinder takes downward screw motion around its own axis. We assume that the cylinder peg and hole are both rigid bodies.

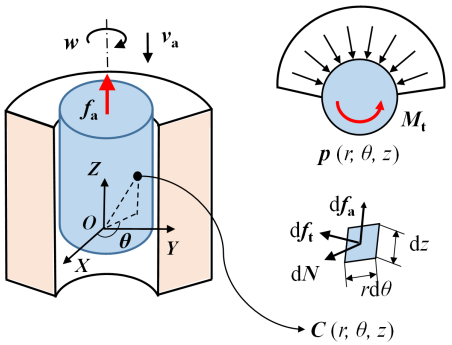

FIGURE 4. Face contact of cylinder and geometry.

In the case of face contact, axial frictional force and tangential frictional force are distributed among the entire contact surface, resulting in a friction wrench $\boldsymbol{W}$ that is composed of a resultant axial friction $\boldsymbol{f}_a$ and a resultant tangential friction moment $\boldsymbol{M}_t$. Wrench describes a force along an axis in space and simultaneously applying a torque about the same axis, denoted as $\boldsymbol{W} = (\boldsymbol{f}_a, \boldsymbol{M}_t)$, and the pitch of wrench h_W can be expressed as:

$$h_W = \frac{\boldsymbol{f}_a \cdot \boldsymbol{M}_t}{\|\boldsymbol{f}_a\|^2} = \frac{M_t}{f_a}. \tag{13}$$

By introducing the cylindrical coordinates (ρ,θ,z) fixed on the cylinder peg, the pressure distributed on contact surface can be represented as $p(r, \theta, z)$. Considering a differential contact surface C, the corresponding differential axial frictional force df_a and differential tangential frictional moment dM_t can be obtained according to Equations(7)(8):

$$df_a = \mu_a p(r, \theta, s) r d\theta dz \tag{14}$$
$$dM_t = r^2 \mu_t p(r, \theta, s) d\theta dz. \tag{15}$$

Hence, the resultant axial friction and tangential friction moment can be expressed as:

$$f_a = \int\int \mu_a p(r, \theta, z) r d\theta dz \tag{16}$$
$$M_t = \int\int r^2 \mu_t p(r, \theta, s) d\theta dz. \tag{17}$$

Combining Equations (9), (10), (16), and (17), we can obtain:

$$\frac{f_a}{M_t} = \frac{\int\int \mu_a p(r, \theta, s) r d\theta dz}{\int\int r^2 \mu_t p(r, \theta, s) d\theta dz} = \frac{\mu_a}{r\mu_t} = \frac{h}{r^2}. \tag{18}$$

Substituting Equations (13) in equation (18), we obtain the following:

$$h_W = \frac{M_t}{f_a} = \frac{r^2}{h}. \tag{19}$$

Equations (16), (18), and (19) show that when the cylinder takes screw motion with face contacts with geometry, the friction wrench is introduced, and the pitch of friction wrench h_W is proportional to the square of cylinder radius r^2 and in inverse ratio to the pitch of screw motion h.

C. SCREW INSERTION WITH AXIAL FRICTION REDUCTION

The previous subsections elaborate on the effect of screw motion on axial friction reduction for situations of both point contact and face contact. With these analysis results, we can obtain the following conclusions for a screw insertion in peg-in-hole assembly:

1) Axial frictional force f_a is equal to the product of normal force N and equivalent friction coefficient μ_a;
2) During screw insertion, keeping a constant axial linear velocity v_a, the axial frictional force f_a can be reduced by decreasing screw pitch h, which means larger angular velocity w;
3) With the same screw pitch h, a larger axial friction reduction can be obtained for larger dimension of mating peg.

To sum up, for a screw insertion in peg-in-hole assembly, we can control the axial friction force by adjusting the screw parameter. In the next two sections, we will discuss the applications of the screw insertion method to clearance-fit and interference-fit peg-in-hole assembly.

III. SCREW INSERTION IN CLEARANCE-FIT PEG-IN-HOLE ASSEMBLY

To verify the influence of screw insertion method on contact situations of clearance-fit peg-in-hole assembly, we will analyze the jamming conditions of both two-point contact and one-point contact states with the quasi-static model. Then the application of robotic peg-in-hole assembly with screw insertion will be discussed.

A. JAMMING CONDITIONS OF SCREW INSERTION

1) TWO-POINT CONTACT

Fig. 5 represents one type of two-point contact during screw insertion, and the peg contacts with the hole at two points simultaneously.

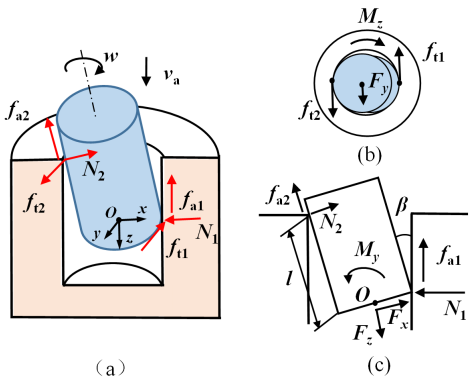

FIGURE 5. Two-point contact state: (a) 3D view, (b) *XOY* plane, (c) *XOZ* plane.

In contrast to the situation of conventional linear insertion, additional tangential friction is introduced during screw insertion and the forces on the peg include insertion forces ($F_x, F_y, F_z, M_x, M_y, M_z$) and contact forces ($N_1, f_{t1}, f_{a1}$) and ($N_2, f_{t2}, f_{a2}$). Considering the low-velocity nature of assembly process, the equilibrium relationships of forces and moments can be derived under quasi-static assumption with equation:

$$\begin{cases} F_x = N_1 \cos\beta - f_{a1} \sin\beta - N_2 \\ F_y = f_{t1} - f_{t2} \\ F_z = N_1 \sin\beta + f_{a1} \cos\beta + f_{a2} \\ M_y = f_{a2} r + N_2 l - N_1 r \sin\beta - f_{a1} r \cos\beta \\ M_z = r f_{t1} + r f_{t2} \end{cases} \tag{20}$$

where l is the insertion depth, β is the tilt angle, and D is the diameter of hole.

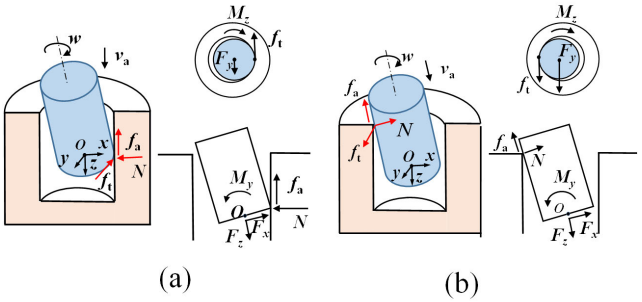

FIGURE 6. Two different situations for one-point contact.

The contacts for peg screw insertion include both situations shown in Fig. 3(a) and Fig. 3(b). Denote the equivalent axial and tangential friction coefficients at two contact points as μ_{a1}, μ_{t1} and μ_{a2}, μ_{t2} respectively. The clearance ratio (the ratio of clearance to diameter) between parts is generally quite small, resulting in tilt angel $\beta \to 0$, where $\sin\beta \approx 0$, $\cos\beta \approx 1$; thus, $\mu_{a1} \approx \mu_{a2} = \mu_a$ and $\mu_{t1} \approx \mu_{t2} = \mu_t$. Substituting this into Equation (20), the jamming condition for two-point contact state can be obtained:

$$\begin{cases} \dfrac{F_x}{F_z} = \dfrac{N_1 - N_2}{\mu_a(N_1 + N_2)} \\ \dfrac{M_y}{rF_z} = m_a \dfrac{F_x}{F_z} + \lambda_a \\ \dfrac{M_z}{rF_y} = \dfrac{N_1 + N_2}{N_1 - N_2} \end{cases} \tag{21}$$

where $m_a = -\frac{l+2\mu_a r}{2r}$, $\lambda_a = \frac{l}{2\mu_a r}$.

2) ONE-POINT CONTACT

Fig. 6 represents two different situations for one-point contact during peg-in-hole screw insertion, in which the peg makes contact with the hole in the inner side surface and the edge of the top surface. During screw insertion, the forces on the peg include insertion forces ($F_x, F_y, F_z, M_x, M_y, M_z$) and contact forces ($N, f_t, f_a$).

For the situation shown in Fig. 6(a), the jamming condition can be derived as:

$$\begin{cases} \dfrac{F_x}{F_z} = \dfrac{1}{\mu_a} \\ \dfrac{M_y}{rF_z} = -1 \\ \dfrac{M_z}{rF_y} = 1. \end{cases} \tag{22}$$

For the situation shown in Fig. 6(b), the jamming condition can be derived as:

$$\begin{cases} \dfrac{F_x}{F_z} = -\dfrac{1}{\mu_a} \\ \dfrac{M_y}{rF_z} = \dfrac{\mu_a r + l}{\mu_a r} \\ \dfrac{M_z}{rF_y} = -1. \end{cases} \tag{23}$$

In contrast to conventional linear insertion, in the *XOY* plane force equilibrium relations are added for screw insertion, where applied force $\boldsymbol{F}_y$ and moment $\boldsymbol{M}_z$ need to keep balance with the tangential friction $\boldsymbol{f}_t$; in the *XOZ* plane the friction coefficient μ is replaced with the equivalent friction coefficient μ_a in Equations (21)-(23) for screw insertion, resulting in changed jamming condition.

B. JAMMING DIAGRAM FOR XOZ AND XOY PLANES

With jamming conditions (21), (22), and (23), jamming diagram of screw insertion for the *XOZ* plane and *XOY* plane can be obtained.

1) JAMMING DIAGRAM FOR XOZ PLANE

Fig. 7 shows the jamming diagram of conventional linear insertion (black solid line) and the jamming diagram of screw insertion (red dashed line).

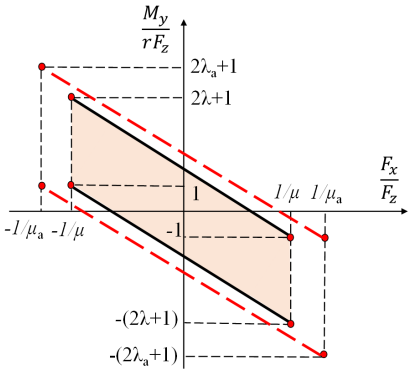

FIGURE 7. Jamming diagram of screw insertion.

The jamming diagram takes the ratio of forces F_x/F_z to $M_y/(rF_z)$ as coordinate axes, forming a close region of quadrangle, and four vertices that represent force equilibrium conditions for one-point contact state, and the top and bottom lines represent the equilibrium conditions for two-point contact state. When the proportion of forces and moments is located in the jamming quadrangle, the peg will slip into the hole; otherwise, the peg will be stuck on the hole.

The jamming diagram describe the feasible region of proportions of forces and moments, and area of feasible region determines the jamming possibility, which can be calculated by the following equation:

$$S = \frac{4\lambda}{\mu}. \tag{24}$$

Combining Equation (21), the relationship of parameters $(\frac{1}{\mu}, \lambda)$ for conventional linear insertion and parameters $(\frac{1}{\mu_a}, \lambda_a)$ for the proposed screw insertion is:

$$\begin{cases} \dfrac{1}{\mu_a} > \dfrac{1}{\mu} \\ \lambda_a > \lambda. \end{cases} \tag{25}$$

Hence, we have $S_{screw} > S_{linear}$, that is, the area of jamming quadrangles of the proposed screw insertion is larger

than that of conventional linear insertion, suggesting that the proposed screw insertion method for peg-in-hole assembly has lower possibility of jamming than that of conventional linear insertion in the XOZ plane.

2) FEASIBLE REGION FOR M_Z AND F_Y IN XOY PLANE

Fig. 8 shows the feasible regions (in dark color) in the XOY plane, describing the constraints for the relationship of moment M_z and force F_y to prevent jamming.

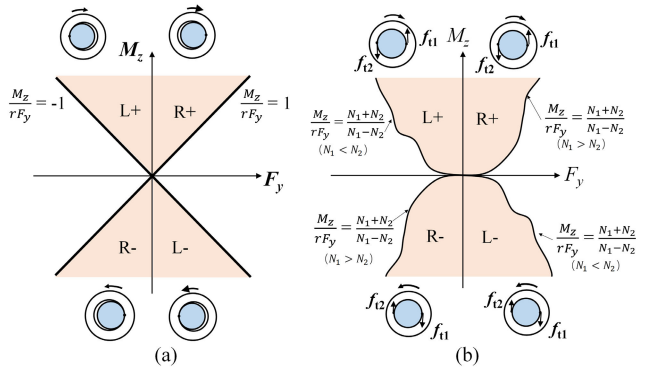

FIGURE 8. Feasible regions for M_Z and F_Y in XOY plane: (a)one-point contact state,(b) two-point contact state.

For one-point contact shown in Fig. 8(a), the feasible regions to prevent jamming are divided into four sections (R+, R−, L+, and L−) according to position of contact points and rotary direction of peg. 'R' represents the right side contact, and 'L' represents the left side contact; '+' represents the peg rotating in positive direction of the Z-axis, and '−' represents the peg rotating in negative direction of the Z-axis.

For two-point contact shown in Fig. 8(b), the feasible regions are divided into four sections (R+, R−, L+, and L−) according to the value of normal forces and rotary direction of peg. 'R' represents the peg contacts with right normal force N_1 larger than left normal force N_2, and 'L' represents the peg contacts with condition $N_1 < N_2$; '+' represents the peg rotating in positive direction of the Z-axis, and '−' represents the peg rotating in negative direction of the Z-axis. It should be noted that, the curve shape of $\frac{M_z}{F_y} = \frac{N_1+N_2}{N_1-N_2}$ is dependent on the variations of normal forces N_1 and N_2.

When M_z and F_y fall in the feasible regions in dark color, the peg can avoid jamming in the XOY plane. It can be seen that the feasible regions for one-point contact and two-point contact are both open regions, which means the area of the feasible region is infinity. The peg will not be stuck in the XOY plane with large enough applied moment M_z, which is generally satisfied for automatic equipment. Therefore, there is no need to consider the jamming problem in the XOY plane for peg-in-hole assembly.

In summary, the jamming analysis for the XOZ and XOY planes prove that the proposed screw insertion method for peg-in-hole assembly has lower possibility of jamming than that of conventional linear insertion.

C. ROBOTIC SCREW INSERTION IN PEG-IN-HOLE ASSEMBLY WITH AXIS OFFSET

Next, we focus on the application of robotic screw insertion to clearance-fit peg-in-hole assembly.

During the robotic assembly process, points on peg could not rotate around the nominal axis due to geometrical errors of the workpiece and kinematic errors of the robots. Therefore, the influence of axis offset on screw insertion should be analyzed.

Consider the situation (see Fig. 9) in which the peg rotates around the axis with geometric deviation to the nominal cylindrical axis. The actual rotary axis intersects the top and bottom face at point A' and A. When the peg rotates angle θ_r around the actual axis, circle O on the bottom surface moves to circle O'. Make a line through point A at angle β_r from X-axis, intersecting the circles at points B and B'.

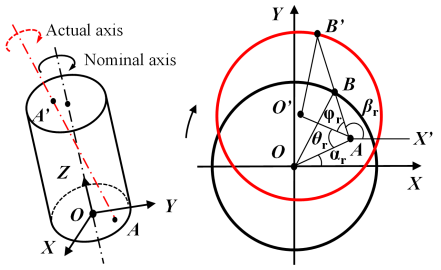

FIGURE 9. Radial variation after rotation with axis offset.

For the sake of simplification, neglect the orientation error between the actual and nominal axis. Assume that the largest offset from points on the actual axis to the nominal axis is d, and it is obtained at point A with angle α_r from X-axis, and then, the radial variations from points on the peg to actual axis in the direction with angle β_r from X-axis after rotation can be expressed by:

$$\begin{aligned}\left|\overline{BB'}\right| &= \left|\overline{AB'}\right| - \left|\overline{AB}\right| \\ &= d\cos\varphi_r + \sqrt{r^2 - d^2 + d^2\cos^2\varphi_r} \\ &\quad - d\cos(\varphi_r + \theta_r) - \sqrt{r^2 - d^2 + d^2\cos^2(\varphi_r + \theta_r)}\end{aligned} \tag{26}$$

where $\varphi_r = \pi - \beta_r - \theta_r$, $\alpha_r, \beta_r \in [-\pi, \pi]$.

When condition $\beta_r = \frac{\pi}{2} + \alpha_r - \theta_r$ is satisfied, $\left|\overline{BB'}\right|$ obtain the maximum value as:

$$\Delta = Max\left|\overline{BB'}\right| = 2d\left|\sin\frac{\theta_r}{2}\right|. \tag{27}$$

Equation (27) shows that when the peg rotates with axis offset, the maximum variation for points on the peg Δ has positive correlation with maximum axis offset d and rotation angle θ_r. If the peg takes continuous screw insertion with $\theta_r > \pi$, maximum radial variation Δ is equal to $2d$. For high-precision peg-in-hole assembly, the tight clearance between the peg and hole is generally smaller than $2d$. To maintain screw insertion, the rotation angle α_r must be

restricted; a feasible motion strategy is reciprocate screw insertion with rotation frequency f_{screw} and amplitude θ_{screw} (see Fig. 10).

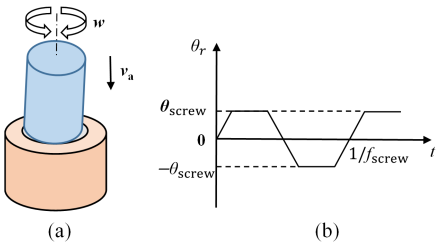

FIGURE 10. Reciprocate screw insertion: (a) peg-in-hole assembly, (b) variations of θ over time.

The reciprocate screw insertion needs to meet following constraints:

1) Mating precision requirement. The maximum radial variation Δ is restricted by the clearance δ of the mating peg and hole with equation:

$$2d\left|\sin\frac{\theta_{screw}}{2}\right| \le k_m\delta \tag{28}$$

where k_m is the mating factor defined in this paper, generally choosing $k_m < 0.3$. When $\theta_{screw} \to 0$, Equation (29) can be simplified as:

$$\theta_{screw} \le k_m\frac{\delta}{d}. \tag{29}$$

2) Inertia matching requirement. The high frequency of reciprocate motion may arouse the mechanical resonance of automation equipment, especially for heavy-weight equipment whose resonance frequency could be tens of Hz. Therefore, the frequency of reciprocate motion f_{screw} needs to be restricted as follows:

$$f_{screw} = \frac{w}{\theta_{screw}} \le k_i f_r \tag{30}$$

where k_i is the inertia matching factor, generally choosing $k_i < 0.3$.

3) Friction reduction requirement. Equations (9) and (12) show that the axial friction reduction is related to screw pitch; to maintain proper axial friction, the screw insertion parameter needs to satisfy condition:

$$\mu_a = \frac{h}{\sqrt{h^2+r^2}}\mu \le k_f\mu \tag{31}$$

where k_f is friction reduction factor with $k_f < 1$. Then, the screw parameter r/h needs to satisfy:

$$\frac{r}{h} \ge \sqrt{\frac{1-k_f^2}{k_f^2}}. \tag{32}$$

Equations (29), (30), and (32) provide the constraints for the reciprocate screw insertion that can be used to choose the proper reciprocate screw insertion parameters to reduce the influence of axis offset.

IV. SCREW INSERTION IN INTERFERENCE-FIT PEG-IN-HOLE ASSEMBLY

With the axial friction reduction of face contact derived in section II, we will discuss the application of screw insertion to interference-fit peg-in-hole assembly with different materials, and the expression of the friction wrench during assembly will be derived.

The actual situation of interference-fit peg-in-hole assembly does not satisfy the assumption of rigid bodies. After part mating, the peg diameter would decrease, while the hole diameter would increase, as shown in Fig. 11.

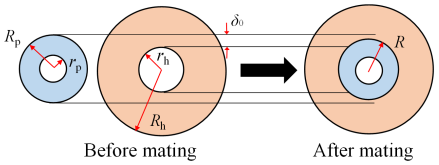

FIGURE 11. Radius of peg and hole with interference fit before/after mating.

Assume that the distribution of the contact pressure p between the peg and hole is only dependent on the radial coordinate ρ; then, the distributed pressure can be expressed by Lame equations [19] for thick-walled cylinders as:

$$p = \frac{\delta_0 E_e}{2R} \tag{33}$$

where $E_e = \frac{2}{\frac{1}{E_h}\left(\frac{R_h^2+R^2}{R_h^2-R^2}-\upsilon_h\right)+\frac{1}{E_p}\left(\frac{R^2+r_p^2}{R^2-r_p^2}-\upsilon_p\right)}$

and

δ_0 is the radial interference between parts;

E_p and E_h are the elastic modulus of the peg and hole, respectively;

υ_p and υ_h are the Poisson ratio of the peg and hole, respectively;

R_p and r_p are the outer and inner radius of the peg before mating, respectively;

R_h and r_h are the outer and inner radius of the hole before mating, respectively; and

R is the radius of parts after mating.

In the case of peg-in-hole assembly, the peg is solid, and we have $r_p = 0$ and $R_h = \infty$; then, E_e can be simplified as:

$$E_e = \frac{2}{\frac{1}{E_h}(1-\upsilon_h)+\frac{1}{E_p}(1-\upsilon_p)} \tag{34}$$

where E_e is only related to the material properties of the parts.

Substituting Equation (33) into Equations (16) and (17), axial resultant friction f_a and tangential friction moment M_t can be calculated by:

$$f_a = \int_0^l\int_0^{2\pi}\mu_a pR d\theta dz = 2\pi\mu_a l E_e\delta_0 \tag{35}$$

$$M_t = \int_0^l\int_0^{2\pi}R^2\mu_t p d\theta dz = 2\pi\mu_t l E_e\delta_0 R \tag{36}$$

where l is the insertion depth.

Equations (35) and (36) show that the friction wrench between interference-fit peg-in-hole assembly is proportional to the elastic modulus of the parts, and the feasibility of screw insertion is closely related to the material of parts.

1) INTERFERENCE FIT OF METAL PARTS

Taking the interference fit between the shaft and roll bearing inner race for example, the elastic modulus reaches to tens of Gpa, and the peg rotating with axis offset will destroy the original mating face between parts, generating a large friction wrench. Therefore, the traditional method of thermal expansion or contraction may be a better choice.

2) INTERFERENCE FIT OF ELASTIC PEG AND INELASTIC HOLE

In the situation in which a peg of elastic material is matted with an inelastic hole, the elastic modulus of the elastic peg is much smaller than that of the hole, and radius of the hole remains unchanged after part mating; therefore, we have the following:

$$M_t = 2\pi\mu_t l E_e \delta_0 r_h \tag{37}$$

$$E_e = \frac{E_p}{1-\upsilon_p}. \tag{38}$$

The equations show that the tangential moment is only related to the radius of inelastic hole and the material property of elastic peg, and E_e is much smaller than that of the mating of metal parts.

Combining Equations (9), (10), (35), and (37), we obtain:

$$h_W = \frac{M_t}{f_a} = \frac{r_h \mu_t}{\mu_a} = \frac{{r_h}^2}{h}. \tag{39}$$

Equation (39) shows that the axial friction reduction of screw insertion still works for the interference fit of elastic peg and inelastic hole, which will be verified in the following experiment section.

Therefore, the interference-fit mating process of the elastic part and inelastic part can be a suitable application for screw insertion. The axial friction reduction of screw insertion from certain aspects accounts for the phenomenon that the stopper of bottle may be easier to be pulled out when the operation is imposed with rotation. To avoid the abnormal behavior due to the rotational and axial movement, particularly in the area nearer to contact points or surfaces, the suggestive materials are the cork materials which are usually used as the stopper of wine bottle, and the rubber materials which can be used for sealing of equipment to keep oil or water.

V. EXPERIMENT

To verify axial friction reduction with screw motion, the experiment of point contact between the peg and rigid plane and screw insertion experiment of both interference-fit and clearance-fit peg-in-hole assembly were carried out. During the experiments, the peg was manipulated with a 6-DOF ABB IRB 1200 robot, and the forces and moments were recorded with an F/T sensor (ABB Sensor 165) installed on the wrist of the robot.

A. EXPERIMENT OF SCREW MOTION WITH POINT CONTACT

The robotic system for point contact between an aluminum peg (size: $\Phi 30$ mm $\times$ 100 mm) and an aluminum contact plane is shown in Fig. 12(a). In the first stage of the experiment, the robot linearly moved the peg along the plane with constant velocity; in the second stage, the peg took a composite motion similar to Fig. 3(b), where the peg moved along the same line and rotates around its own axis uniformly and simultaneously. The process was repeated with different screw parameters ($r/h = 0.3, 0.6, 1, 0.2, 15, 2, 3, 4$), and the axial linear velocity v_a was 0.1 mm/s.

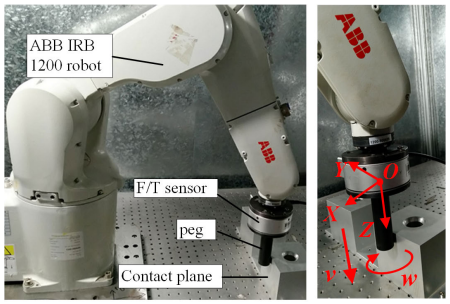

(a)

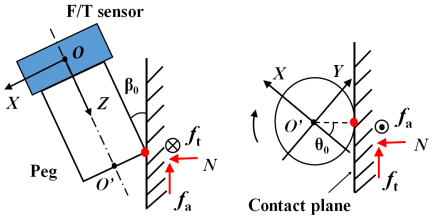

(b)

FIGURE 12. Point contact experiment: (a) setup, (b) force analysis diagram.

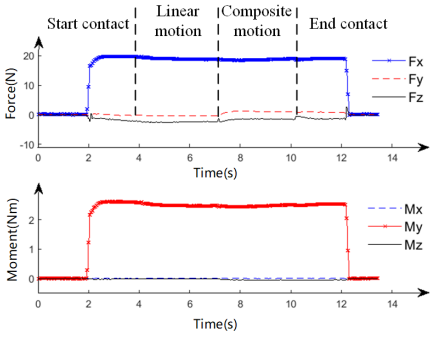

FIGURE 13. Force/moment data with screw parameter $r/h = 1.2$ in each motion stage.

Fig. 13 shows the force/moment data with screw parameter $r/h = 1.2$ in each motion stage. As shown in Fig. 12(b), the relationship of N, f_a, f_t and measured force can be expressed with equations:

$$\begin{cases} F_x = N\cos\beta_0\cos\theta_0 - f_a\sin\beta_0\cos\theta_0 + f_t\sin\theta_0 \\ F_y = -N\cos\beta_0\sin\theta_0 + f_a\sin\beta_0\sin\theta_0 + f_t\cos\theta_0 \\ F_z = -N\sin\beta_0 - f_a\cos\beta_0. \end{cases} \tag{40}$$

During the experiments, β_0 was set to 0.5°, and θ_0 was calibrated with force/moment data, thus, the equivalent axial friction coefficient μ_a and the equivalent tangential friction coefficient μ_t can be calculated.

Fig. 14(a) shows the values of the equivalent friction coefficients μ_a and μ_t changing from the linear motion stage to composite motion stage. It can be seen that, in composite motion stage, the resultant friction is reallocated with an introduced tangential friction $\boldsymbol{f}_t$, resulting in decreased μ_a and increased μ_t. The results demonstrate the effectiveness of friction reallocation method for axial friction reduction proposed in Section II.

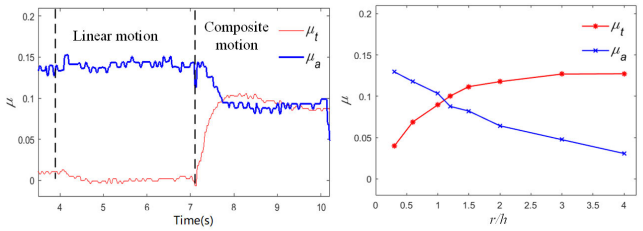

FIGURE 14. Variations of μ_a and μ_t: (a) for screw parameter $r/h = 1.2$ in linear and composite motion stage, (b) for different screw parameter r/h in composite motion stage.

Fig. 14(b) shows the variations of μ_t and μ_a with respect to screw parameter r/h. It can be seen that when the screw parameter r/h increases, μ_a decreases, and μ_t increases, and the magnitude of variations become larger. The results are identical to the axial friction reduction of screw motion with point contact described by Equations (9) and (10).

Table 1 provides the comparison of the ratio of measured equivalent friction coefficients $k' = \frac{\mu_t}{\mu_a}$ and the ratio of theoretical equivalent friction coefficients $k = \frac{r}{h}$. The results are in good agreement with Equation (6) that the ratio of axial friction f_a and tangential friction f_t is proportional to the pitch h and in inverse ratio to radius r.

TABLE 1. Results for Φ30 mm aluminum peg with $v_a = 0.1$ mm/s.

k	$\theta_r(°)$	$w(°/s)$	μ_t	μ_a	k'	$k'/k(\%)$
0.3	0.3438	0.1146	0.0398	0.1296	0.307	102.43
0.6	0.6876	0.229	0.0691	0.1178	0.587	97.85
1	1.146	0.382	0.0896	0.1034	0.867	86.66
1.2	1.3752	0.4584	0.1003	0.0878	1.143	95.25
1.5	1.719	0.573	0.1117	0.0821	1.361	90.70
2	2.292	0.764	0.1177	0.0643	1.831	91.57
3	3.438	1.146	0.1269	0.0475	2.669	88.98
4	4.584	1.528	0.1272	0.0308	4.134	103.39

In order to test the influence of velocity, material and radius of peg on the axial friction reduction, three groups of experiments were implemented with different screw parameter r/h, as shown in Fig. 15, and Table 2 shows the variations of μ_t and μ_a with respect to screw parameter r/h and the comparison of the measured and theoretical ratio k' and k.

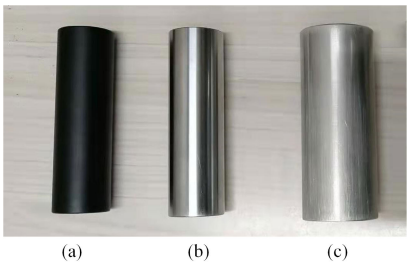

FIGURE 15. Different pegs: (a) Φ30mm aluminum peg, (b) Φ30mm steel peg, (c) Φ40mm aluminum peg.

TABLE 2. Results for screw motion with different velocity, material and radius of peg.

Setting	k	μ_t	μ_a	k'	$k'/k(\%)$
Φ30 mm Aluminum 0.05 mm/s	0.3	0.0375	0.1249	0.273	91.15
	0.6	0.0671	0.1118	0.557	92.86
	1	0.0922	0.0922	0.897	89.68
	2	0.1166	0.0583	1.671	83.53
	3	0.1237	0.0412	2.782	92.72
Φ30 mm Steel 0.1 mm/s	0.3	0.0508	0.1492	0.341	113.63
	0.6	0.0701	0.1121	0.626	104.29
	1	0.0978	0.1086	0.901	90.08
	2	0.1190	0.0667	1.784	89.19
	3	0.1171	0.0421	2.781	92.71
Φ40 mm Steel 0.1 mm/s	0.3	0.0467	0.1504	0.310	103.42
	0.6	0.0677	0.1221	0.554	92.36
	1	0.0905	0.0935	0.967	96.72
	2	0.1070	0.0601	1.781	89.04
	3	0.1197	0.0432	2.772	92.39

The good experimental results show that the axial friction reduction of screw motion is effective for different axial linear velocity, material and radius of the peg, which demonstrate the robustness of screw insertion method.

In summary, the experimental results of screw motion with point contact well verify the effect of screw motion on axial friction reduction derived in Section II.

B. EXPERIMENT OF SCREW INSERTION IN INTERFERENCE-FIT PEG-IN-HOLE ASSEMBLY

Fig. 16 shows the robotic peg-in-hole assembly system for a rubber taper workpiece peg (size: Φ29-Φ34 mm, hardness: 65 Shore A) and an aluminum workpiece hole (size: Φ30 mm×60 mm). The peg-in-hole assembly was implemented by the conventional position control, and the peg was manipulated in two motion strategies (linear insertion and the reciprocate screw insertion).

The process was repeated with screw different parameters shown in Table 3, which were chosen according to Equations (29), (30), and (32), insertion velocity v_a was 2 mm/s,and reciprocate frequency f_{screw} was 1.11 Hz. To avoid large position and orientation errors between the axis of the rubber taper peg and the axis of the steel hole, the trajectory of screw insertion was calibrated beforehand.

Fig. 17 shows force/moment data with screw parameter $r/h = 1$; the screw insertion process was performed in the

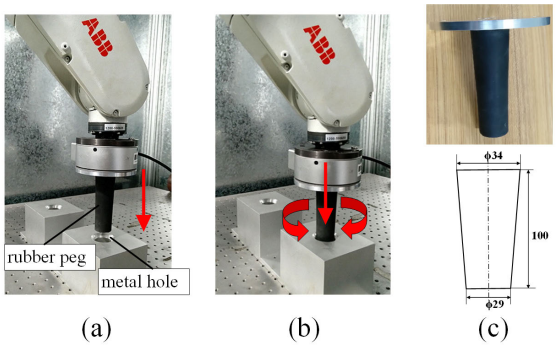

FIGURE 16. Setup for interfrence-fit peg-in-hole assembly: (a) linear insertion, (b) screw insertion, (c) rubber taper workpiece peg.

TABLE 3. Parameters of reciprocate screw insertion.

No.	r/h	$w(^\circ/s)$	$\theta_{screw}(^\circ)$
1	0	0	0
2	0.3	2.55	0.573
3	0.6	5.1	1.146
4	1	8.49	1.91
5	2	16.98	3.82
6	4	33.96	7.64

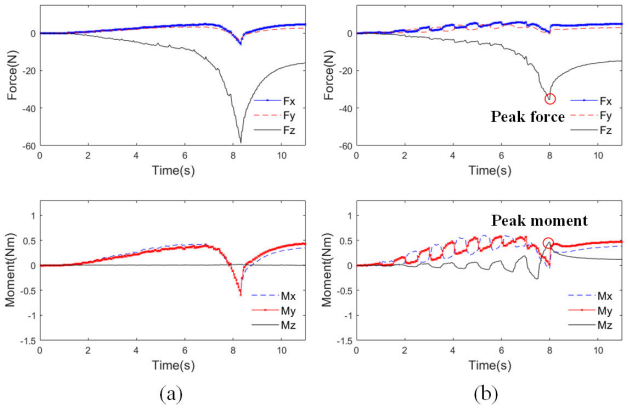

FIGURE 17. Force/moment data for linear insertion (a) and screw insertion with $r/h = 1$ (b).

0-8 s stage, and then, the peg maintains stationary. During the insertion, Z direction bears most of the contact friction, and according to the equilibrium relationship, F_z reflects the value of the resultant axial friction $\boldsymbol{f}_a$ and M_z reflects the value of the resultant friction moment $\boldsymbol{M}_t$. Reciprocate screw insertion results in the periodic fluctuation of the forces and moments. Deeper insertion makes the magnitude of $\boldsymbol{f}_a$ and M_t increase substantially, which is because tighter mating of the taper peg causes larger contact pressure between parts.

Table. 4 shows force/moment data with different screw parameter r/h. To eliminate the influence of periodic variations The axial friction f_a and tangential moment M_t in the table take values in the peak force of F_z and peak moment of M_z, respectively; then, the actual pitch of friction wrench

TABLE 4. Results for reciprocate screw insertion.

r/h	$M_t(N\cdot m)$	$f_a(N)$	$h'_W(mm)$	$h_W(mm)$	$R_h(\%)$
linear	0	58.73	0	0	100
0.3	0.202	54.8	3.686	4.5	81.94
0.6	0.357	46.22	7.724	9	85.82
1	0.465	34.45	13.498	15	89.98
2	0.761	27.34	27.835	30	92.78
4	1.514	26.24	57.698	60	96.16

$h'_W = M_t/f_a$, and the matching rate R_h is the ratio of actual to nominal friction wrench pitch.

It can be seen that, when the screw parameter r/h increases, the resultant axial friction $\boldsymbol{f}_a$ decreases, and the resultant tangential moment $\boldsymbol{M}_t$ increases substantially. The results are identical to the axial friction reduction of screw motion with face contact described by Equations (9), (10), (16), and (17). The matching rates show good agreement with Equations (19) and (39) that the pitch of friction wrench h_W is proportional to the square of cylinder radius r^2 and in inverse ratio to the pitch of screw motion h.

In summary, the experimental results well verify the axial friction reduction of reciprocate screw insertion for interference-fit peg-in-hole assembly. The peg was tapered in experiments for convenience of inserting a peg with larger radius into a hole, it should be noted that the effects also work for the non-tapered peg because the constant radius of metal hole is the parameter that really matters according to Equation (39).

C. EXPERIMENT OF SCREW INSERTION IN CLEARANCE-FIT PEG-IN-HOLE ASSEMBLY

Fig. 18 shows the robotic system for the assembly of an aluminum workpiece peg (size: Φ29.96 mm) and an aluminum workpiece hole (size: Φ30 mm), and the clearance is 0.04 mm. The robotic assembly process was implemented by the impedance control, and the peg was inserted into the hole in two different motion strategies, that is the conventional impedance control with linear insertion and the revised impedance control with reciprocate screw insertion.

1) IMPEDANCE CONTROL WITH DIFFERENT MOTION STRATEGIES

For conventional impedance controlled peg-in-hole process, the position errors between the peg and hole were compensated with force/moment errors measured from the F/T sensor

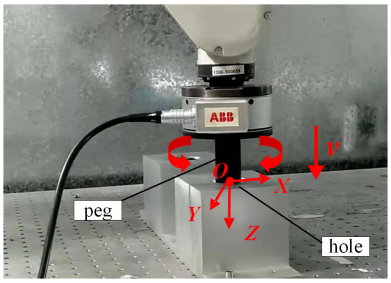

FIGURE 18. Setup for clearance-fit peg-in-hole assembly.

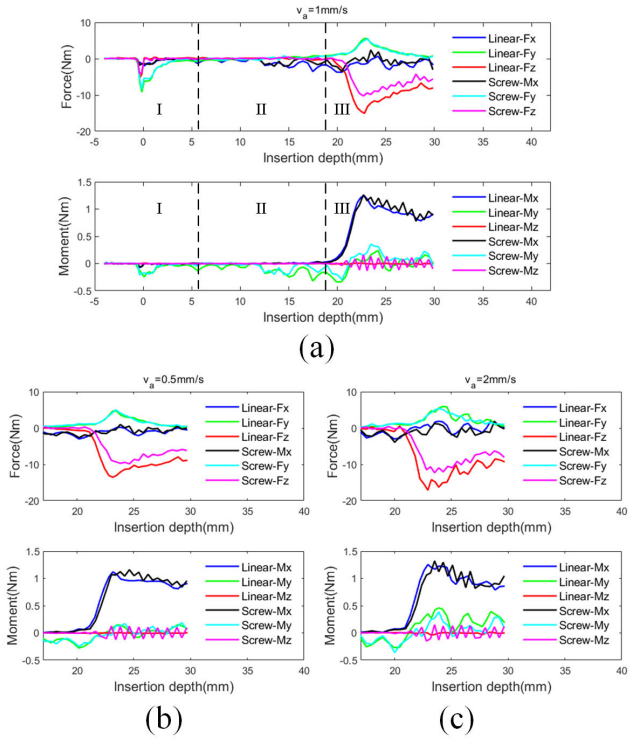

FIGURE 19. Force/moment with respect to insertion depth for linear and screw insertion: (a) $v_a = 1$ mm/s, (b) $v_a = 0.5$ mm/s in large contact stage, (c) $v_a = 2$ mm/s in large contact stage.

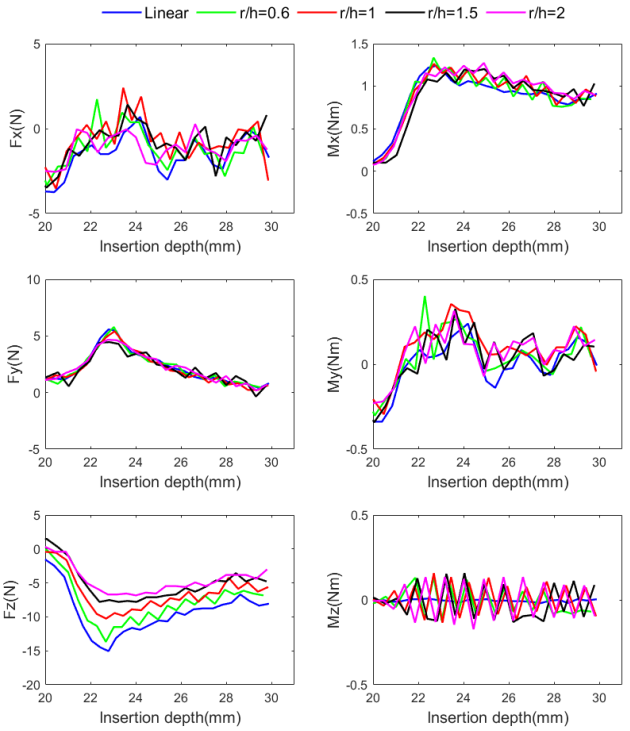

FIGURE 20. Force/moment data in large contact stage for linear and reciprocate screw insertion with $r/h = 0.6, 1, 1.5, 2$.

by equation:

$$\Delta \boldsymbol{P} = \boldsymbol{K_e}(\boldsymbol{F} - \boldsymbol{F_{ref}}) + \boldsymbol{B_e}(\dot{\boldsymbol{F}} - \dot{\boldsymbol{F}}_{\boldsymbol{ref}}) \tag{41}$$

where $\Delta \boldsymbol{P} = (\Delta x, \Delta y, \Delta z, \Delta \theta x, \Delta \theta y, \Delta \theta z)$ is the increment motion, $\boldsymbol{K_e} = diag\{k_x, k_y, k_z, k_{\theta x}, k_{\theta y}, k_{\theta z}\}$ is the stiffness matrix, and $\boldsymbol{B_e} = diag\{b_x, b_y, b_z, b_{\theta x}, b_{\theta y}, b_{\theta z}\}$ is the damping matrix.

During linear insertion process, the contact moment M_z is almost 0, so the corresponding increment rotation angle $\Delta\theta_z$ for each motion step is almost 0.

In contrast, the increment rotation angle $\Delta\theta_z$ for the reciprocate screw insertion is revised to construct the screw motion, and the rotation angle round the insertion direction for each motion step can be expressed by:

$$\Delta\theta_{zi} = \begin{cases} \dfrac{\Delta z}{h}, & i = 1, 3, 5, \cdots \\ -\dfrac{\Delta z}{h}, & i = 2, 4, 6, \cdots \end{cases} \tag{42}$$

where i is the motion step number. The frequency of reciprocate screw motion depends on the increment insertion depth Δz and insertion velocity v_a.

During the experiments, the control parameters were set: transitional stiffness $k_x = k_y = 0.006$, $kz = 0.01$, rotational stiffness $k_{\theta x} = k_{\theta y} = k_{\theta z} = 0.003$, damping matrix $\boldsymbol{B_e} = 0$, and the reference force $\boldsymbol{F}_{ref} = (0, 0, -50\ N, 0, 0, 0)$. The insertion depth was set to 30mm, which was measured from the bottom of chamfer along the axis of the hole, the reciprocate screw parameters were chosen according to the constraints of Equations (29), (30), and (32), and screw pitch h and insertion velocity v_a were the variables for experiments.

2) EXPERIMENTAL RESULTS

Fig. 19 (a)-(c) show the force/moment data with different insertion velocities ($v_a = 0.5$ mm/s, 1 mm/s, and 2 mm/s) after each motion step of linear insertion and reciprocate screw insertion. The assembly process can be divided into three stages: (I) chamfer-cross, (II) small contact, and (III) large contact. In large contact stage, it can be seen that the differences in F_x,F_y,M_x,M_y,M_z between the two motion strategies are small, while the insertion force F_z for reciprocate screw insertion, which reflects the axial frictional force, is evidently reduced compared with that for linear insertion, and the change law is not affected by the changing insertion velocities. And the small changes of other forces and moments demonstrate the feasibility of screw insertion method for clearance-fit assembly, as discussed in Section III.C.

In order to test the influence factor of axial friction reduction, the reciprocate screw insertion experiments with different screw parameters ($r/h = 0.6, 1, 1.5, 2$) were implemented with constant insertion velocity ($v_a = 1$ mm/s). And the force/moment data after each motion step in large contact stage are shown in Fig. 20, and the results for linear insertion are shown in the blue line for comparison. It can be seen that,

TABLE 5. Results for peg-in-hole assembly with different r/h.

r/h	$\overline{F}_z$(N)	$\overline{R'}_{F_z}$(%)	R_{F_z}(%)
linear	-11.12	0	0
0.6	-9.58	83.6	85.7
1	-8.17	73.7	70.7
1.5	-6.63	61.7	55.5
2	-5.75	50.4	44.7

the curves of force F_x, F_y and moment M_x, M_y, M_z fluctuate across the blue line (linear insertion) in a small range for different r/h. Compared with linear insertion, the insertion force F_z is evidently reduced for all reciprocate screw insertions, and the gap increases with larger r/h. The results are consistent with the analysis of Section II.A.

For quantitative analysis of the screw insertion method, the experiments with different screw parameters were repeated for 10 times, and the average $\overline{F}_z$ in 22-28 mm depth are shown in Table 5. The results indicate that the average reduction rate $\overline{R'}_{F_z}$ of F_z accords basically with the theoretical value R_{F_z} calculated by Equation (7) and (9).

In summary, the above experimental results well verify the axial friction reduction for reciprocate screw insertion for clearance-fit peg-in-hole assembly.

VI. CONCLUSION

This paper proposes the screw insertion method for peg-in-hole assembly which combines the screw motion strategy with the conventional motion control approach, resulting in reduced axial frictional force and better contact situations for mating process, which is well verified by the results of the point contact experiment and screw insertion experiment of both interference-fit and clearance-fit peg-in-hole assembly.

For transition-fit peg-in-hole assembly, which is also a common type of engineering fit, the actual contact state is either clearance fit or interference fit; therefore the axial friction reduction of screw motion derived above still works in the case of transition fit. Furthermore, although the above-mentioned frictions are sliding frictions, axial friction reduction still works for the maximum static friction. The derivation of axial static friction reduction is similar to that of sliding friction. Compared with only applying a pushing force, the cylinder workpiece is easier to move by imposing a pushing wrench, including an axial moment and a pushing force.

The radial variation of points due to rotary axis offset has some influence on the friction reduction, especially for high-precision peg-in-hole assembly. To address this problem, it may be possible to reduce the influence by real-time axis correction strategies using force/moment data from the F/T sensor. This is the future work that we will focus on.

REFERENCES

[1] D. E. Whitney, *Mechanical Assemblies: Their Design, Manufacture, and Role in Product Development*. New York, NY, USA: Oxford Univ. Press, 2004.
[2] Z. Hou, M. Philipp, K. Zhang, Y. Guan, K. Chen, and J. Xu, "The learning-based optimization algorithm for robotic dual peg-in-hole assembly," *Assem. Automat.*, vol. 38, no. 4, pp. 369–375, 2018.
[3] S. Simunovic, "Force information in assembly processes," in *Proc. 5th Int. Symp. Ind. Robots*, Sep. 1975, pp. 415–431.
[4] D. E. Whitney, "Quasi-static assembly of compliantly supported rigid parts," *J. Dyn. Syst., Meas., Control*, vol. 104, no. 1, pp. 65–77, 1982.
[5] Y. Fei and X. Zhao, "Jamming analyses for dual peg-in-hole insertions in three dimensions," *Robotica*, vol. 23, pp. 83–91, Jan. 2005.
[6] K. Zhang, J. Xu, H. Chen, J. Zhao, and K. Chen, "Jamming analysis and force control for flexible dual peg-in-hole assembly," *IEEE Trans. Ind. Electron.*, vol. 66, no. 3, pp. 1930–1939, Mar. 2019.
[7] N. Pitchandi, S. P. Subramanian, and M. Irulappan, "Insertion force analysis of compliantly supported peg-in-hole assembly," *Assem. Autom.*, vol. 37, no. 3, pp. 285–295, 2017.
[8] M. H. Raibert and J. J. Craig, "Hybrid position/force control of manipulators," *J. Dyn. Syst., Meas., Control*, vol. 103, no. 2, pp. 126–133, 1981.
[9] N. Hogan, "Impedance control: An approach to manipulation: Part I—Theory," *J. Dyn. Syst., Meas., Control*, vol. 107, no. 1, pp. 1–7, 1985.
[10] H. Park, J.-H. Bae, J.-H. Park, M.-H. Baeg, and J. Park, "Intuitive peg-in-hole assembly strategy with a compliant manipulator," in *Proc. IEEE ISR*, Oct. 2013, pp. 1–5.
[11] S. R. Chhatpar and M. S. Branicky, "Search strategies for peg-in-hole assemblies with position uncertainty," in *Proc. IEEE/RSJ Int. Conf. Intell. Robots Syst. Expanding Soc. Role Robot. Next Millennium*, vol. 3, Oct./Nov. 2001, pp. 1465–1470.
[12] R. Li and H. Qiao, "Condition and strategy analysis for assembly based on attractive region in environment," *IEEE/ASME Trans. Mechatronics*, vol. 22, no. 5, pp. 2218–2228, Oct. 2017.
[13] L. Balletti, A. Rocchi, F. Belo, M. Catalano, M. Garabini, G. Grioli, and A. Bicchi, "Towards variable impedance assembly: The VSA peg-in-hole," in *Proc. 12th IEEE-RAS Int. Conf. Humanoid Robots (Humanoids)*, Nov./Dec. 2012, pp. 402–408.
[14] B. Baksys, J. Baskutiene, and S. Baskutis, "The vibratory alignment of the parts in robotic assembly," *Ind. Robot*, vol. 44, no. 6, pp. 720–729, 2017.
[15] D. Godfrey, "Vibration reduces metal to metal contact and causes an apparent reduction in friction," *A S L E Trans.*, vol. 10, no. 2, pp. 183–192, 1967.
[16] S.-S. Yoo and D.-E. Kim, "Effect of vibration on friction reduction in dry and lubricated sliding conditions," in *Proc. 5th World Tribol. Congr. (WTC)*, vol. 3, Jan. 2014, pp. 2696–2697.
[17] M. A. Chowdhury and M. M. Helali, "The effect of amplitude of vibration on the coefficient of friction for different materials," *Tribol. Int.*, vol. 41, no. 4, pp. 307–314, 2008.
[18] P. Gutowski and M. Leus, "The effect of longitudinal tangential vibrations on friction and driving forces in sliding motion," *Tribol. Int.*, vol. 55, pp. 108–118, Nov. 2012.
[19] A. Liuti, F. R. Vedugo, N. Paone, and C. Ungaro, "Monitoring techniques for high accuracy interference fit assembly processes," *AIP Conf.*, vol. 1740, no. 1, 2016, Art. no. 060005.

ZHI LIU received the B.E. degree in mechanical engineering from Central South University, Changsha, China, in 2010. He is currently pursuing the Ph.D. degree with the Department of Mechanical Engineering, Tsinghua University, Beijing, China. His research interests include robot calibration, manufacturing automation, and robotic force control.

LIBIN SONG received the B.E. and Ph.D. degrees in mechanical engineering from Tsinghua University, Beijing, China, in 2000 and 2008, respectively.

He is currently an Assistant Professor with the Department of Mechanical Engineering, Tsinghua University, Beijing, China. His research fields include advanced manufacturing, special robot, and biomedical instruments.

ZHIMIN HOU received the B.E. degree in mechanical engineering from Tongji University, Shanghai, China, in 2016. He is currently pursuing the master's degree in mechanical engineering with Tsinghua University, Beijing, China.

He was a Visiting Scholar with the Department of Computing Science, University of Alberta, Edmonton, Canada, in 2018, advised by Prof. R. S. Sutton. His research interests include reinforcement learning, machine learning, robotic force control, and intelligent control.

KEN CHEN received the Ph.D. degree in mechanical engineering from Zhejiang University, Hangzhou, China.

He is currently a Professor with the Department of Mechanical Engineering, Tsinghua University, Beijing, China. His research interests include robotics and intelligent control, humanoid robots, microrobots and small robots, medical and space robots, manufacturing automation systems, and hydraulic servo systems.

SHAOLI LIU received the B.S. degree in mechanical engineering from the Beijing Institute of Technology, Beijing, China, in 2007, and the Ph.D. degree in mechanical engineering from Tsinghua University, Beijing, China, in 2012. She is currently an Associate Professor with the School of Mechanical Engineering, Beijing Institute of Technology, Beijing, China. Her research interests include machine vision, image processing, and intelligent inspection.

JING XU (M'12) received the B.E. degree in mechanical engineering from the Harbin Institute of Technology, Harbin, China, in 2003, and the Ph.D. degree in mechanical engineering from Tsinghua University, Beijing, China, in 2008. He was a Postdoctoral Researcher with the Department of Electrical and Computer Engineering, Michigan State University, East Lansing, MI, USA. He is currently an Associate Professor with the Department of Mechanical Engineering, Tsinghua University. His research interests include vision-guided manufacturing, image processing, and intelligent robotics.